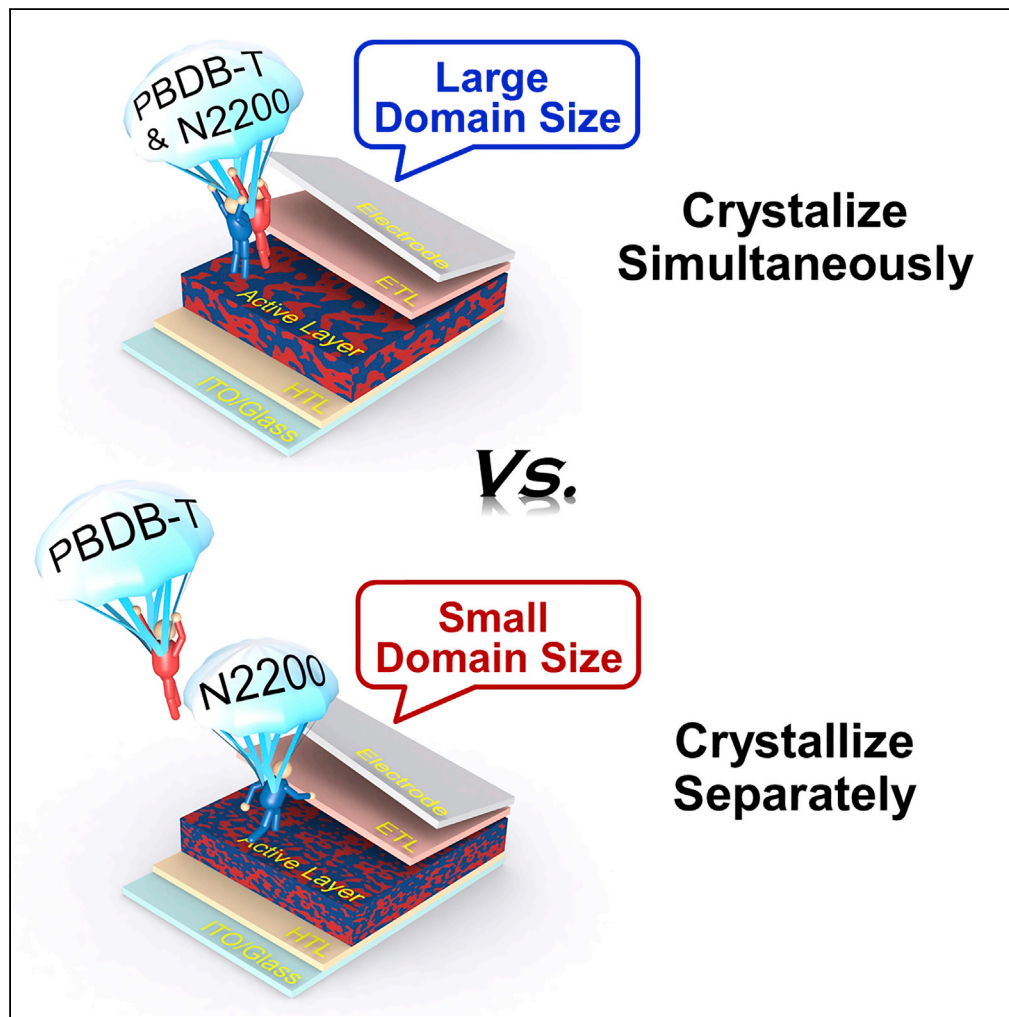## Article

Domain size control in all-polymer solar cells

Jiangang Liu,
Yukai Yin, Kang
Wang, ...,
Chunpeng Song,
Qiuju Liang, Wei
Huang

drcpsong@hotmail.com (C.S.)
qiujuliang@nwpu.edu.cn (Q.L.)
iamwhuang@nwpu.edu.cn
(W.H.)

Highlights

This strategy decreases
domain size without
sacrificing crystallinity

A phase diagram about
solution state and domain
size was proposed

Article

Domain size control in all-polymer solar cells

Jiangang Liu,[1] Yukai Yin,[1] Kang Wang,[1] Puxin Wei,[1] Haodong Lu,[1] Chunpeng Song,[1,*] Qiuju Liang,[1,2,*] and Wei Huang[1,*]

SUMMARY

In all polymer solar cells (all-PSCs), the domain size is critical for device performance. In highly crystalline polymer blends, however, precisely adjusting the domain size remains a significant challenge because of the simultaneous crystallization of both components. Herein, a strategy that promotes acceptor and donor to crystallize separately was proposed. Take PBDB-T/N2200 blends for instance; the solution state and confined crystallization were combined, which induced the crystallization of N2200, and PBDB-T occurred during the film-forming process and at thermal annealing stage. This separated crystallization process lowers the driving force of phase separation without affecting the degree of crystallinity of the blends. Thus, an interpenetrating network with high crystallinity and proper domain size was obtained, which boosted the power conversion efficiency to 7.59%. Importantly, the relation between pre-aggregation and domain size was established, which may be a guide to precisely adjust the active layer's domain size in all-PSCs.

INTRODUCTION

All-polymer solar cells (all-PCSs), which are composed of a polymeric electron donor and polymeric electron acceptor, are gaining popularity (Zhang et al., 2020, 2021a; Song et al., 2020), thanks to the advancement in material design, interface engineering, and morphology control. Besides, recent advancements also demonstrate a rapid rise in power conversion efficiency (PCE) of over 15% for all-PSCs (Luo et al., 2020; Fu et al., 2020, 2021; Fan et al., 2021; Ma et al., 2021; Sun et al., 2021; Zhang et al., 2021b). Despite the rapid process in PCE, the device stability of solar cells is also a key factor for commercial applications. Compared to small molecules, the diffusivity of polymers is relatively low, which could suppress the formation of large-scaled phase separation during their practical application. Moreover, the long-chain polymers prefer to run through different crystalline regions, which invested the active layer with continuous paths and mechanical flexibility (Zhou et al., 2022). Because of these characteristics, all-PSCs exhibit better stability compared with polymer/fullerene or polymer/nonfullerene-based solar cells, which indicate that all-PSCs hold a great potential applications in large-area flexible devices (Zhang and Li, 2021; Xu et al., 2019; Liu et al., 2020a).

Considerable research works have demonstrated that the morphology of all-PCSs bulk heterojunction (BHJ) systems is one of the key parameters to achieve PCE. It is widely approved that the morphology of active layer in efficient all-PCSs should be an interpenetrating network with approximated 10–20 nm domains, which is optimal for efficient charge generation and transport (Lee et al., 2016; Liang et al., 2017; Neupane et al., 2017; Ye et al., 2019a; Zhu et al., 2019).

However, when compared to all-small molecule or polymer/small molecule blends, achieving such small domain size in all-PSCs is very difficult because of their thermodynamic and kinetic properties (Liu et al., 2020b). In terms of thermodynamics, polymers play a little role in the entropy increase when they are mixed because of their large molecular weights; therefore, the donor and acceptor tend to phase separate and form large sized domains (Liu et al., 2017; Veenstra et al., 2007). In the kinetic aspect, the polymer's glass transition temperature of polymer is relatively low, allowing it polymer to rearrange in the late stage of the film-forming process, which further increases the scale of phase separation (Gu et al., 2016). As a result, the majority of all-PSCs reported have relatively large domain sizes, and it have lagged significantly in PCE behind the corresponding polymer/nonfullerene counterparts (Liu et al., 2017; Mori et al., 2018; Zhang et al., 2018, 2021c).

To suppress the phase separation, a variety of methods through regulating the complicated kinetic and thermodynamic factors have been applied. According to the Lifshitz–Slyozov law, the domain size grows as the coarsening time increases (Binder and Stauffer, 1976). As a result, lowering the phase separation
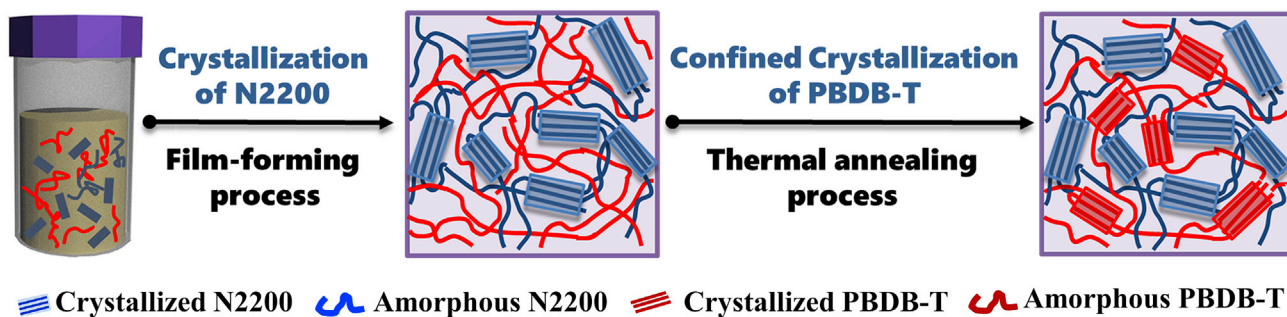
[1]Northwestern Polytechnical University, Xi'an 710129, China

[2]Lead contact

*Correspondence:
drcpsong@hotmail.com (C.S.),
qiujuliang@nwpu.edu.cn (Q.L.),
iamwhuang@nwpu.edu.cn (W.H.)

https://doi.org/10.1016/j.isci.2022.104090

Scheme 1. Schematic diagram for the modulated crystallization process

time is efficient to reduce domain sizes. Kim et al. studied the relationship between domain size and boiling point of solvent, and the results showed that the degree of phase separation reduced with the decrease of the solvent's boiling point, *i.e.*, the domain size is ca. 27 nm produced by chloroform and 170 nm produced by *o*-dichlorobenzene (Lee et al., 2016). Similarly, increasing the temperature of substrates and the spin rate can shorten the film-forming process as well, forcing molecules to be frozen at metastable state with smaller domain sizes (Zhang et al., 2018, 2021d; Zhao et al., 2020; Li et al., 2021).

Manipulating the thermodynamic parameters to adjust the interaction between donor and acceptor is also effective to reduce the domain size. To control the solubility parameter of polymers, Bao et al. synthesized a sequence of donor and acceptor polymers with varying quantities of polystyrene side chains to regulate the solubility parameter of polymers (Kurosawa et al., 2018). The results showed that attaching polystyrene side chains on acceptor polymers could increase the compatibility between donor and acceptor, which decreased the degree of phase separation and enhanced device performance. Using a compatibilizer as a solid additive could enhance the interaction between donor and acceptor. Sommer et al. employed a donor—acceptor block copolymers (BCP), which has good interaction with both donor and acceptor, to reduce the domain size of a PCDTBT/P3HT blend film. They found that with increasing amounts of BCP, the domain size reduced from several micrometers to tens of nanometers; moreover, a thermodynamically stable morphology was also obtained (Lombeck et al., 2016).

The phase separation is mainly induced by the crystallization; hence, reducing the intrinsic crystallinity of the active layer can suppress the degree of phase separation efficiently. Enhancing the steric hindrance (Kang et al., 2015), increasing the molecular weights (Kang et al., 2015), or synthesizing polymer with much more flexible backbone (Li et al., 2016) can reduce polymer's crystallinity of polymer. Wang and the coauthors modulated the crystallinity of N2200 by substituting the single thiophene units for a portion of bithiophene units in the backbone. The introduction of single thiophene units destroyed the regularity and increased the backbone disorder. Thus, a lower crystallinity of acceptor and higher miscibility between donor and acceptor were obtained, which resulted in nanostructured morphology with smaller domain size (Li et al., 2016). Besides, elevating the temperature of solution could reduce the crystallinity, thus obtaining a reduced domain size as well. According to the theory of Flory and recent research, the aggregation of polymer in solution could be suppressed by elevating solution temperature (Reichenberger et al., 2018). The aggregates act as nucleus during the film-forming process, and promote the crystallization no matter in polymer/fullerene or polymer/nonfullerene blend systems (Chen et al., 2021; Li et al., 2021; Liu et al., 2014). For example, Liu et al. studied the relationship between solution state and phase separation (Wang et al., 2019, 2020). Take the CD1/PBN-12 blend system for instance; they elevated the temperature of solution from 30°C to 90°C, leading to a smaller domain size and optimal crystallinity. Consequently, the PCE of the device is enhanced from 7.7% to 10.0% (Wang et al., 2020). Although the approaches discussed above can reduce the domain size, yet they all come at the expense of active layer's crystallinity. Although high crystallinity is necessary for all-PCSs to obtain excellent device performance, because it is crucially important for not only photon absorption but also exciton dissociation and charge transport (Liu et al., 2020b; Song et al., 2018). Thus, it is urgent to deepen the understanding of phase separation principles and devise rational strategies for generating a highly crystalline active layer with fine phase separation structure.

In this work, we combined the aggregating behavior of polymer in solution and confined crystallization during thermal annealing (TA) process to modulate the crystallization kinetics in highly crystalline PBDB-T/N2200
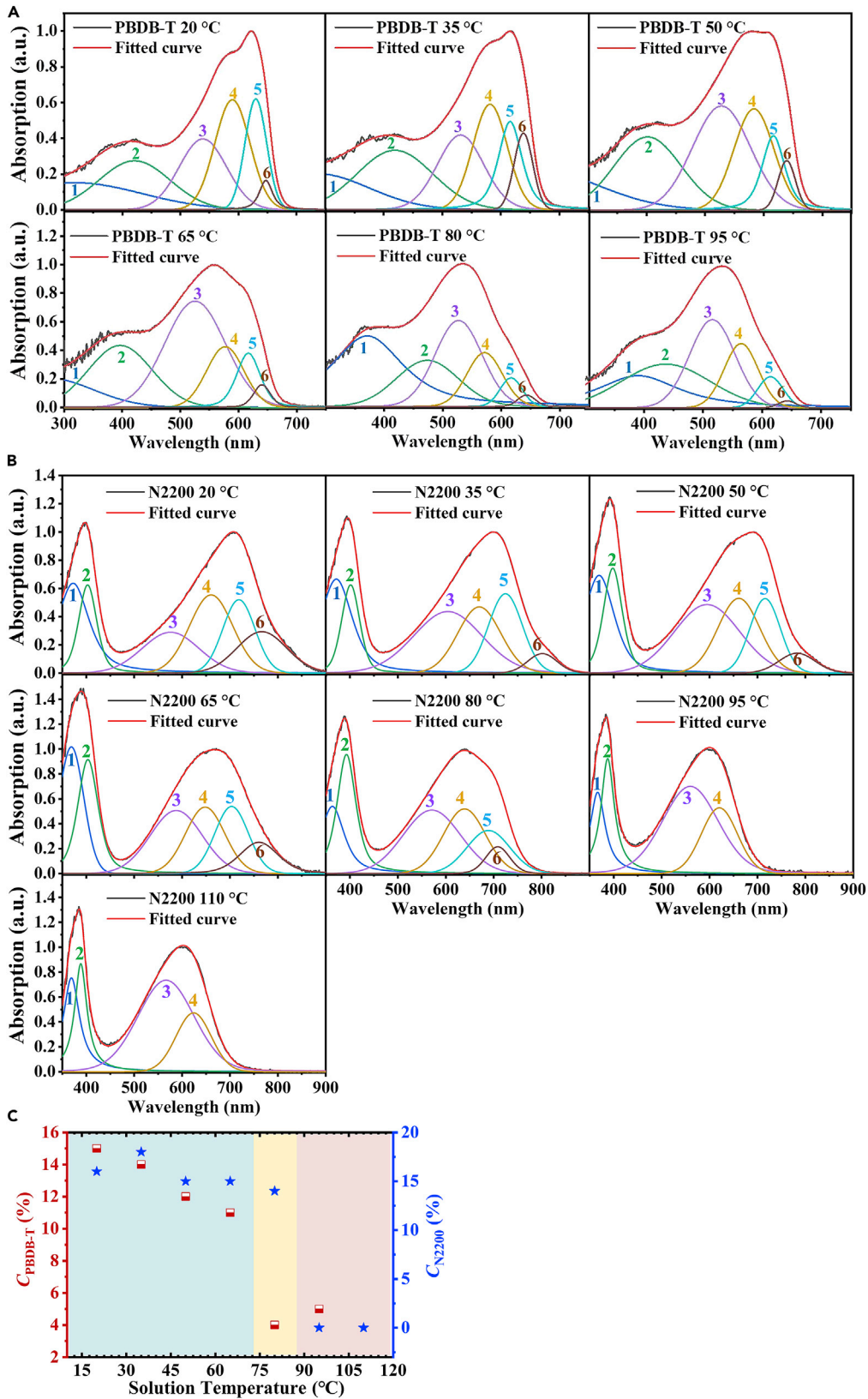
Figure 1. The aggregated behavior of PBDB-T and N2200 in solution
(A and B) Experimental and simulated absorption spectra of PBDB-T and N2200 in solution at different temperatures.
(C) The pre-aggregate contents of PBDB-T and N2200 in solution at different temperatures.

blends, which suppressed the degree of phase separation without the expense in crystallinity of active layer. In particular, N2200 formed pre-aggregates in PBDB-T/N2200 solution by adjusting the solution temperature, permitting N2200 to crystallize and form crystalline framework during the film-forming process. On this basis, TA treatment was employed, which induced PBDB-T to further crystallize under the confinement of the N2200 crystalline network. Because of the separated crystallization process of donor and acceptor, the driving force of phase separation was weakened. As a result, an interpenetrating network with high crystallinity and fine domains were fabricated. The optimal morphology facilitated the exciton dissociation and carrier transport, resulting in a PCE of 7.59%, which is the highest photovoltaic performance for the PBDB-T/N2200-based all-PSCs processed without additives.

RESULTS AND DISCUSSION

To suppress the degree of phase separation without expensing crystallinity, the crystallization kinetics of PBDB-T/N2200 blends was modulated, *i.e.*, N2200 crystallized during film-forming process, whereas PBDB-T suffered from confined crystallization because of the presence of N2200 crystalline framework at post TA stage as shown in Scheme 1.

Temperature-dependent aggregation behaviors of PBDB-T and N2200

Owing to the coplanarity of PBDB-T and N2200 (Liu et al., 2020b), both of them tend to form pre-aggregates in solution under ambient temperature. The pre-aggregates act as nuclei, which induce the crystallization of both PBDB-T and N2200 during the film-forming process because of the "memory effect". In our strategy, the aggregation of PBDB-T was inhibited by regulating the solution temperature; consequently, crystallization of PBDB-T during the film-forming process was suppressed. Hence, the crystallization processes of PBDB-T and N2200 were separated.

The π-π interaction among conjugated polymers is a prerequisite for forming aggregates in solution, which are mainly governed by the solvent-polymer affinities (χ_{S-P}) (Liu et al., 2017; Ye et al., 2019b). When the value of χ_{S-P} is big, polymer chains in solvent tend to interact with the homogenesis rather than with solvent molecules to reduce energy, which results in the formation of aggregates. Conversely, if the value of χ_{S-P} is small, the polymers are prone to interact with solvent molecules, thus the polymers can be dispersed in the solvent at molecular-level. As shown in Equation (1):

$$\chi_{S-P} = V\left(\Delta\delta_d^2 + 0.25\Delta\delta_p^2 + 0.25\Delta\delta_h^2\right) / RT \qquad \text{(Equation 1)}$$

where V is the solvent molar volume, $\Delta\delta_d$, $\Delta\delta_p$, and $\Delta\delta_h$ are the differences of dispersion, polar, and hydrogen bonding solubility parameters for the solvent and polymer, respectively. R is the gas constant and T is the absolute temperature. The value of χ_{S-P} is inversely proportional to the temperature of solution in a certain system (Machui and Brabec, 2013). Hence, the aggregated state in solution could be tuned by regulating the solution temperature.

In accordance with Spano's method (Spano, 2010; Spano and Yamagata, 2011), we employed UV-vis spectra to analyze the aggregating behavior of polymers in solution. As shown in Figure 1A, there are peaks centered at 580 and 620 nm for PBDB-T at ambient temperature, which is ascribed to π-π* transition along intrachain and between interchain, respectively (Qian et al., 2012). When the solution's temperature was elevated from 20 to 80°C, the intensity of the peak at 620 nm disappeared gradually; meanwhile, the peak centered at 580 nm blued shifted to 530 nm. The absorption spectra remained almost unchanged, when the solution temperature was elevated further (Steyrleuthner et al., 2012). This phenomenon indicates that PBDB-T aggregates strongly in CB solution at 20°C, and its aggregation could be suppressed effectively through elevating the solution temperature above 80°C (to compare the difference in peak position, the combined UV-vis spectra of solution at different temperature are shown in Figure S1).

To further qualify the contents of pre-aggregates of PBDB-T (C_{PBDB-T}) in solution, the Gaussian vibronic peaks were used to fit the spectra. The fitted peaks labeled 5 (centered at 620 nm) represent the ordered stacking of PBDB-T chains as shown in Figure 1A. Hence, it is rational to use the percentage of
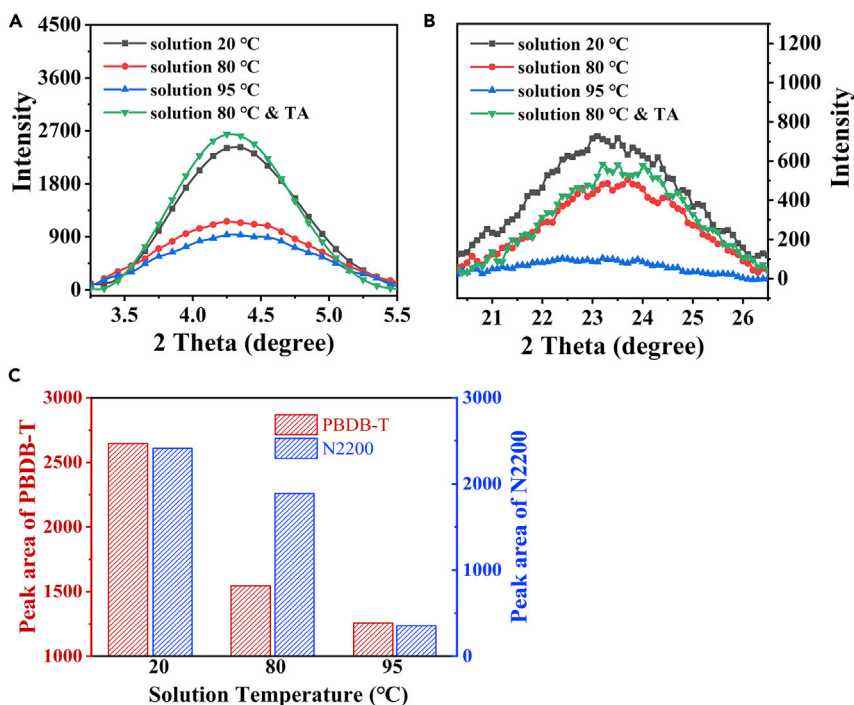
Figure 2. The crystallization behavior of PBDB-T/N2200 films

(A and B) GIXD patterns (1 0 0) diffraction signals of PBDB-T (0 1 0) diffraction signals of N2200 in Film I, Film II, Film III, and Film II with TA.

(C) The area of PBDB-T and N2200 diffraction signals for PBDB-T/N2200 films processed from solution with different temperatures.

peak (labeled 5) area to represent the content of aggregates in solution, *i.e.*, $C_{PBDB-T} = A_5/A_t$, in which $A_t = A_1 + A_2 + A_3 + A_3 + A_4 + A_5 + A_6$. The peak areas and C_{PBDB-T} at different temperatures are summarized in Table S1. According to the fitting results, C_{PBDB-T} vs solution temperature was plotted as shown in Figure 1C. It is obvious that the C_{PBDB-T} dramatically decreases when the solution temperature is above 80°C, which indicates that PBDB-T molecules exist in an amorphous state at high temperature. Here, a critical temperature T_c is defined: when the solution temperature is below T_c, the pre-aggregates exist in the solution, while if the solution temperature is above T_c, there is almost no pre-aggregate. Hence, the T_c for PBDB-T in solution ($T_{c:PBDB-T}$) is defined as 80°C.

As for N2200 solution at ambient temperature, the absorption spectrum is characterized by two spectral features, a high-energy band at 390 nm attributed to the π-π* transition and a low-energy band at 710 nm ascribed to the charge-transfer (CT) transition (Figure 1B) (Steyrleuthner et al., 2012). Raising the temperature induces a continuous blue shift of the long-wavelength absorption. When the temperature is above 95°C, the position of this absorption band keeps centered at 570 nm without change. The spectral changes are similar to the solvatochromism of N2200, which indicates the transformation of N2200 from aggregated state to dispersed state (Steyrleuthner et al., 2012). Analogously, the Gaussian vibronic peaks were used to fit the spectra of the N2200 solution as well, and the peak labeled 5 (centered at 710 nm) was used to represent the contents of pre-aggregates in the N2200 solution (C_{N2200}). It is worth noting that when the solution temperature is above 95°C, four Gaussian vibronic peaks were used to fit the absorption curves because of the disappearance of aggregates. The curve of C_{N2200} vs solution temperature is shown in Figure 1C, from which we can infer the T_c of N2200 ($T_{c:N2200}$) is 95°C (the C_{N2200} at different temperatures are summarized in Table S2).

The influence of solution states on film morphology

According to the T_c of PBDB-T and N2200, the aggregated behavior of solution can be divided into three different states with the variation of temperature, and different backgrounds are used to guide the eye as
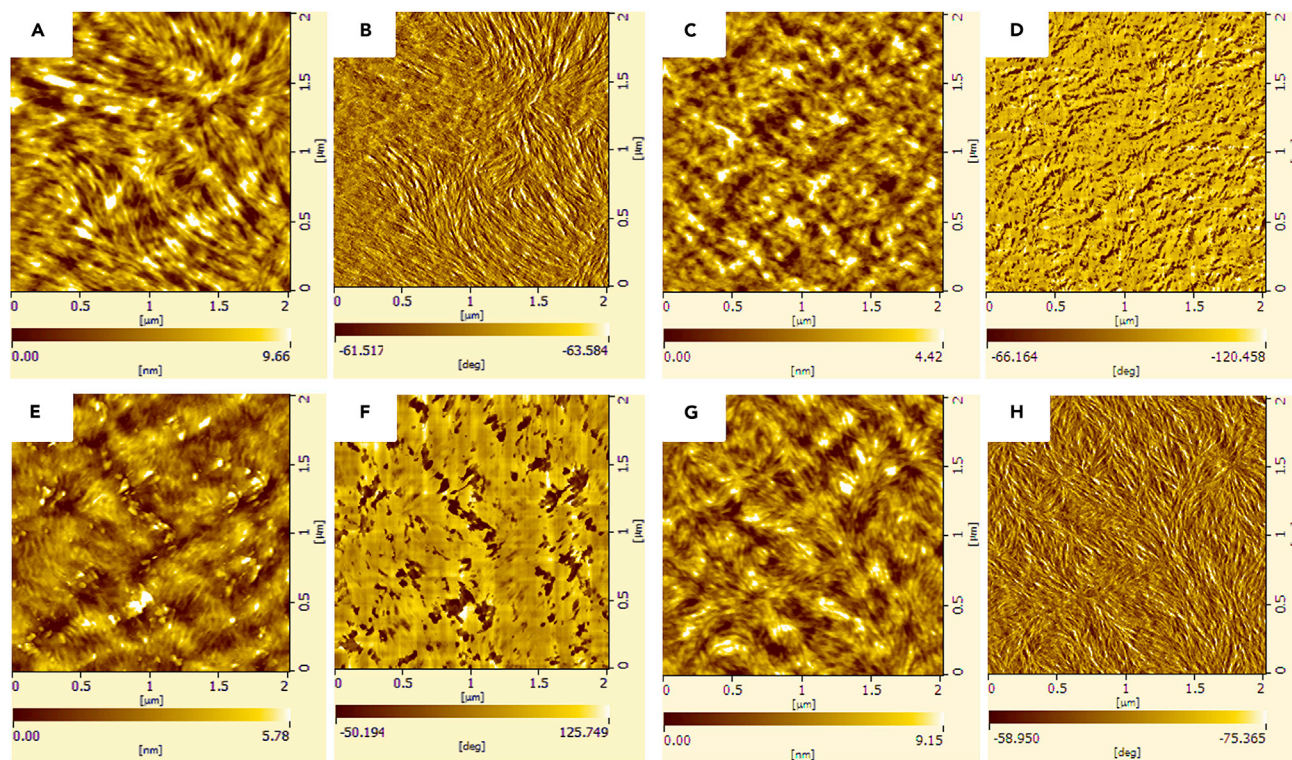
Figure 3. Surface morphology of PBDB-T/N2200 films

(A, C, E, and G) Tapping-mode AFM height images of Film I, Film II, Film III, and Film II with TA at 140°C.

(B, D, F, and H) Tapping-mode AFM phase images of Film I, Film II, Film III, and Film II with TA at 140°C.

shown in Figure 1C. When the solution temperature of PBDB-T/N2200 is below $T_{c:PBDB-T}$ (blue region), both PBDB-T and N2200 form pre-aggregates in solution. If the temperature is above $T_{c:PBDB-T}$ and below $T_{c:N2200}$ (yellow region), only N2200 form pre-aggregates; however, most of PBDB-T disperses in an amorphous state. Elevating the solution temperature above the T_c of $T_{c:N2200}$ (red region), neither PBDB-T nor N2200 form pre-aggregates.

The solution states have great influence on the crystallinity of solid-state films because of the "memory effect". The existence of pre-aggregates would induce the crystallization during the film-forming process, leading to a highly crystalline film. On the contrary, this crystallization process could be suppressed in the absence of pre-aggregates in solution. As shown in Figure S2A, the neat PBDB-T film that I processed from the PBDB-T solution at 20°C displays well-ordered (100) lamellar diffraction ($2\theta = 4.7°$), which means PBDB-T has a high crystallinity. When the film is processed from the PBDB-T solution at 80°C, the peak intensity is (100) reduced, indicating the crystallization is almost suppressed. The processed from the N2200 solution at 20°C, it has high crystallinity as evidenced by the obvious π-π stacking signal ($2\theta = 23.0°$) and high peak intensity, whereas the peak intensity reduced when the film is processed from the N2200 solution at 95°C as shown in Figure S2B. Hence, regulating the solution temperature is an efficient method to modulate the crystallization kinetics of PBDB-T/N2200 blend, *i.e.*, the crystallization of PBDB-T and N2200 occur simultaneously or at different stages (Liu et al., 2014; Ma et al., 2015; Eastham et al., 2017). According to Figure 1C, three solution temperature were selected to study the relationship between crystallization kinetics and morphology of the active layer, including 20°C (Solution I), 80°C (Solution II), and 95°C (Solution III), which belong to three different solution states.

To assess the impact of the pre-aggregation on the crystallinity of blend films, out-of-plane grazing incidence X-ray diffraction (GIXD) measurement was applied. For the blend film processed from the Solution I (Film I), both the lamellar peaks of PBDB-T ($2\theta = 4.7°$) and π-π stacking signals of N2200 ($2\theta = 23.0°$) persist (Figure 2), indicating a high crystallinity of PBDB-T and N2200. As we know, the peak area can represent the degree of crystallinity; therefore, the corresponding peak areas were calculated to quantitatively describe
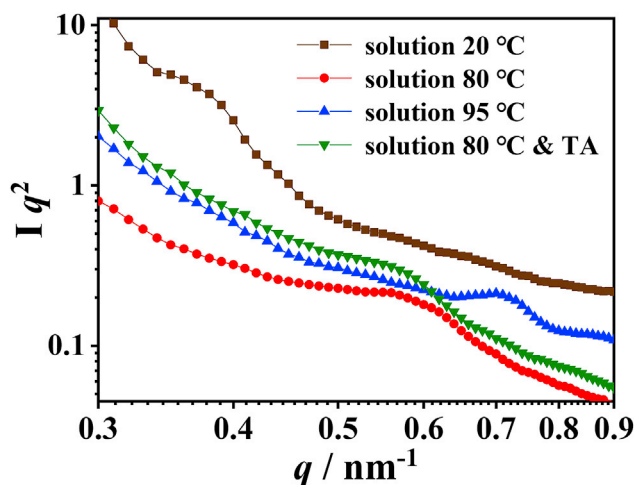
Figure 4. The GISAXS spectra of Film I, Film II, Film III, and Film II with TA at 140°C

the variation trend of crystallinity. The peak area of PBDB-T ($A_{\text{Film I:PBDB-T}}$) is 2647 and the peak area of N2200 ($A_{\text{Film I:N2200}}$) is 2413. Inversely, the crystallization of both PBDB-T and N2200 in Film III (processed from solution III) was suppressed, which could be deduced from the dramatically reduced peak areas ($A_{\text{Film III:PBDB-T}}$ = 1256, $A_{\text{Film III:N2200}}$ = 353). For Film II, the crystallinity of N2200 is high ($A_{\text{Film II:N2200}}$ = 1889), whereas that of PBDB-T is low ($A_{\text{Film II:PBDB-T}}$ = 1546), which suggests only N2200 crystallized and PBDB-T's crystallization was suppressed during spin-coating.

The different crystallization behaviors in three films should be ascribed to the difference of aggregating state of polymers in solution. As is well-known, crystallization is basically dominated by the nucleation and crystal growth process (Liu et al., 2018; Reiter, 2014; Liang et al., 2019). Therefore, ordered pre-aggregates in solution would act as nucleus for the residual polymer molecules to crystallize during the spin-coating, which reduces the energy barrier of nucleation, thus leading to a highly crystalline film. This phenomenon was also reported in other systems when the solution underwent aging, adding additives or the film was fabricated by blading (Liu et al., 2013; Bi et al., 2018; Sen et al., 2018). On the contrary, in the absence of pre-aggregates in solution, the polymer chains would undergo conformational transition, interchain interaction, and the removal of unfavorable configurations during nucleation process, which increases energy barrier of nucleation, thus inhibiting the crystallization of polymers (Muthukumar, 2004).

Crystallization is a kind of driving force for phase separation (Li et al., 2016; Chou et al., 2013). As shown in Figure 2C, the driving force of Film I is the biggest because of its high crystallinity ($A_{\text{Film I}} = A_{\text{Film I:PBDB-T}} + A_{\text{Film I:N2200}}$ = 5060), whereas the one of Film II and Film III decrease gradually according to the reduced crystallinity ($A_{\text{Film II}}$ = 3435, $A_{\text{Film III}}$ = 1690). The reduced driving force indicates lower extent of phase separation, which is confirmed by atomic force microscopy (AFM). For Film I, large fibrous domains pervade in the entire film with a large mean-square surface roughness (rms = 2.54 nm) (Figures 3A and 3B), indicating large domain sizes. For the Film II, due to the suppressed crystallization of PBDB-T, only slender nanofibers of N2200 can be observed (Figures 3C and 3D), and the rms decreases to 1.20 nm. In the Film III, it formed blurred and relatively homogeneous morphology, meanwhile, the smallest value of rms was obtained (1.05 nm) (Figures 3E and 3F). The decreased rms indicates the reduced domain size, which can be further confirmed by grazing-incidence small-angle X-ray scattering (GISAXS). The signal of Film I centers at 0.37 nm^{-1} (Figure 4), and its domain size (d) can be calculated by the equation $d = 2\pi/q$, which is 16.9 nm. For the Film II and Film III, the peak position shifts to 0.58 nm^{-1} and 0.72 nm^{-1}, matching to the domain size of 10.8 and 8.7 nm, respectively.

Above all, it is obvious that the crystallization kinetics was modulated by tuning the solution state, which further affects the domain size of PBDB-T/N2200 solid film. We summarized the relation between the solution states, crystallization behavior and phase separation structure as Scheme 2. When the solution temperature is below $T_{\text{c:PBDB-T}}$, both PBDB-T and N2200 form pre-aggregates in solution. Thus, PBDB-T and
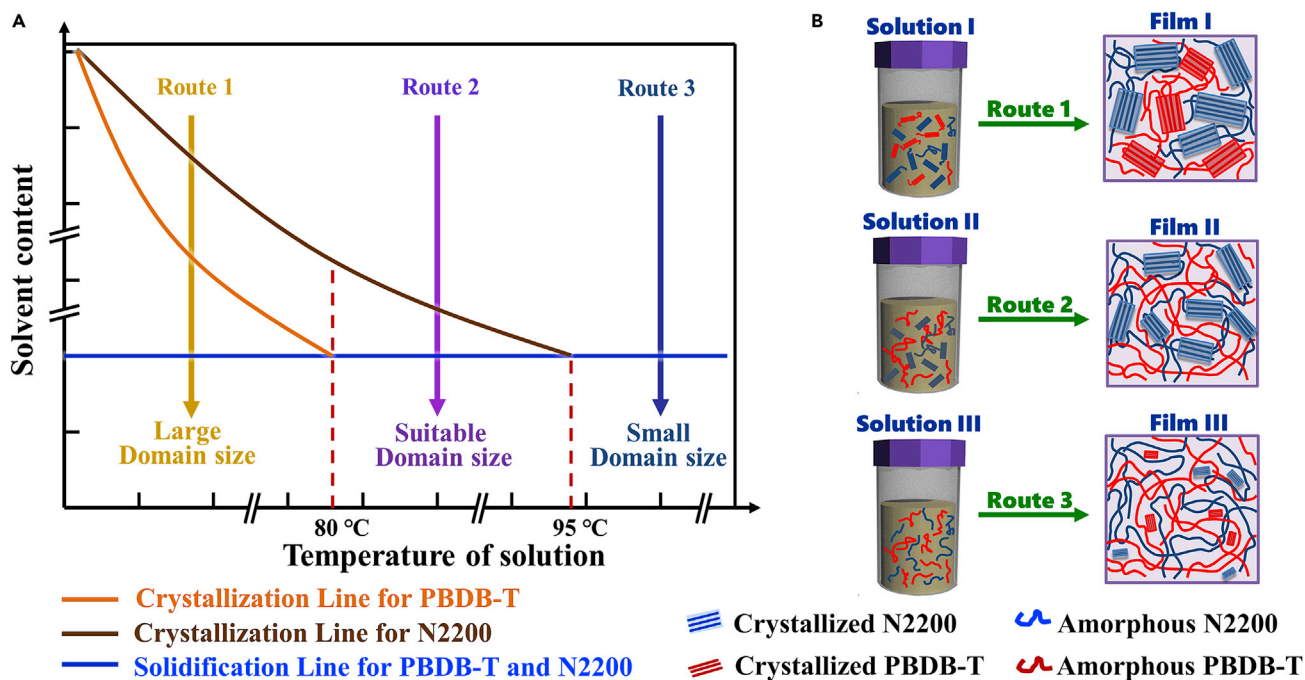
Scheme 2. Illustration of the influence of pre-aggregation on film morphology
(A) The phase diagram of solidification processes for PBDB-T/N2200 solution with different temperatures.
(B) The cartoon of solution states of PBDB-T/N2200 at different temperatures, and the phase separation structures of Film I, Film II, and Film III.

N2200 incline to crystallize simultaneously in the process of spin-coating, which drives the film to form a large domain size (Route 1). On the contrary, if the solution temperature is above $T_{c:N2200}$, neither PBDB-T nor N2200 aggregate in solution. As a result, PBDB-T and N2200 tend to form an amorphous state in the process of spin-coating, thus the domain size is small because of the small phase separated driving force (Route 3). If the solution temperature is between $T_{c:PBDB-T}$ and $T_{c:N2200}$ (80°C ≤ T < 95°C), N2200 forms pre-aggregates, while PBDB-T disperses in an amorphous phase in solution. During the film-forming process, only N2200 crystallizes, leading to an intermediate driving force for phase separation. Consequently, a suitable domain size can be obtained (Route 2).

Confined crystallization of PBDB-T

Besides domain size, the crystallinity is also a crucial factor in determining the device performance. Because it is assumed that high crystallinity will effectively increase charge mobility and consequently improve device performance (Mori et al., 2018; Ye et al., 2017). As previously stated, although the domain size of Film II is proper, PBDB-T in this film is mainly in an amorphous state. The low crystallinity of PBDB-T led to imbalanced charge transport and serious bimolecular recombination, which can be revealed by the current density-voltage (*J-V*) curves as shown in Figure S3 and Table S3.

Hence, the crystallization of PBDB-T should be improved via TA under the confinement of N2200 crystalline framework (Liang et al., 2017; Zhang et al., 2016). To realize this process, the TA temperature was elaborately selected. As shown in Figure 5, we characterized the degree of crystallinity of PBDB-T and N2200 after TA treatment under different temperatures, and the peak area was used to represent its degree of crystallinity. After fitting the peak areas, the evolution of crystallinity of PBDB-T and N2200 vs TA temperature was plotted in Figure 5C. It is obvious that the crystallinity of N2200 remained almost the same, which means the TA process could not trigger the crystallization of N2200, thus its crystalline framework was untouched during the TA process (purple region: 60°C–220°C). However, for PBDB-T, the crystallization behavior shows three different states: from 60°C to 100°C (blue region), PBDB-T was in glassy state and the chains were in frozen state, thus the temperature of TA below 100°C cannot facilitate the crystallization of PBDB-T. From 100°C to 180°C (yellow region), PBDB-T is in high-elastic state and the rearrangement
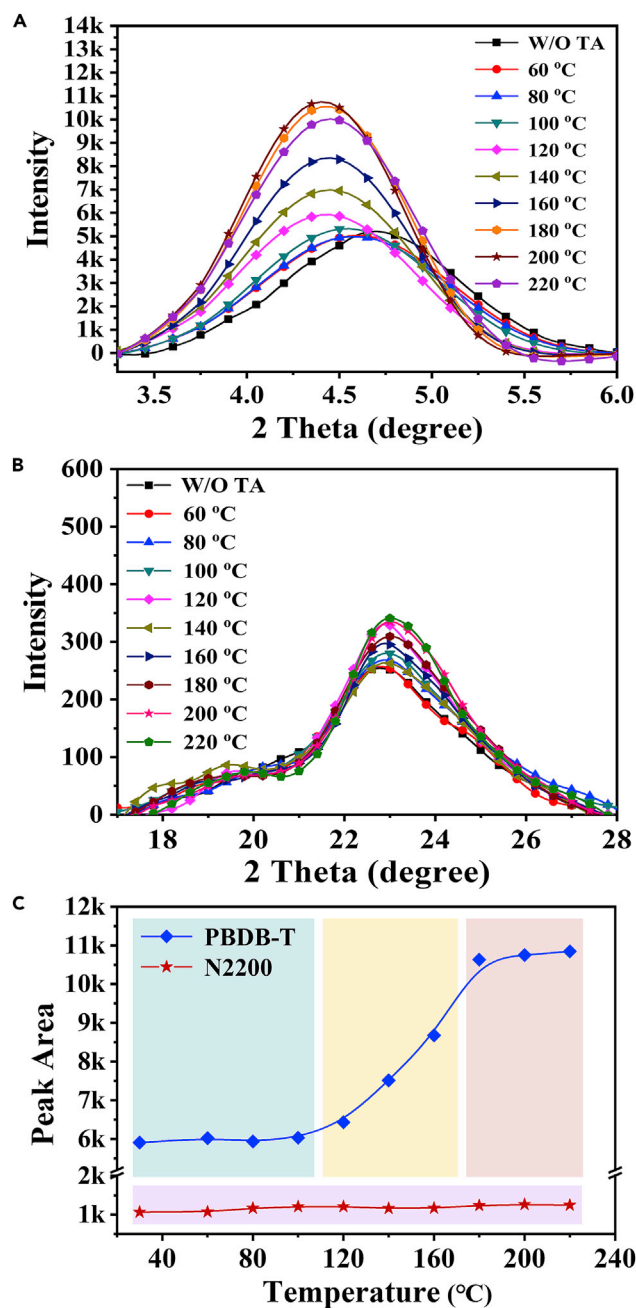
Figure 5. Temperature dependence of crystallinity for PBDB-T and N2200
(A and B) GIXD patterns of neat PBDB-T films and neat N2200 films after TA treatment.
(C) The variation of GIXD peak areas vs TA temperature.

ability of chain segments is promoted as the increasing temperature, thus the crystallinity gradually increases. When the TA temperature is above than 180°C (pink region), the PBDB-T is in molten state and the whole molecule movement is motivated, resulting in the maximum crystallinity (Liang et al., 2018).

The diffusivity of PBDB-T during TA treatment determines whether the PBDB-T crystallizes in a confined manner or not (Zhang et al., 2016). When the temperature of TA is below 100°C, the rearrangement of PBDB-T is almost forbidden, thus the crystallization of PBDB-T cannot be triggered (Figure S4A). Although the temperature of TA is over 180°C, the crystallization of PBDB-T breaks out of the confinement of N2200

Table 1. Photovoltaic properties of Sim-Device and Sep-Device

Devices	V_{oc}(V)	J_{sc}(mA/cm^2)	FF	PCE$_{max}$(%)	PCE(%)	μ_h (cm^{2}v^{-1}s^{-1})	μ_e (cm^{2}v^{-1}s^{-1})
Sim-Device	0.85 ± 0.01	10.86 ± 0.19	0.64 ± 0.01	6.07	5.91 ± 0.16	2.64×10^{-4}	7.12×10^{-5}
Sep-Device	0.83 ± 0.01	13.48 ± 0.20	0.67 ± 0.01	7.59	7.38 ± 0.21	4.53×10^{-3}	2.34×10^{-4}

The average values of PCE are calculated from 16 devices.

because of the strong molecular diffusivity (Zhang et al., 2016). Consequently, the phase separation structure was destroyed, resulting in a large domain size (Figure S4B). When the temperature of TA is between 100°C and 180°C, the conformation of chain segments could adjust in the crystalline frame of N2200, thus the PBDB-T suffers from confined crystallization. Hence, the TA temperature was set as 140°C. After TA treatment, the crystallinity of PBDB-T was improved significantly (Figure 2). Meanwhile, the domain size is kept in suitable range, which can be confirmed by the AFM and GISAXS (Figures 3 and 4). As a consequence, an interpenetrating network with high crystallinity and proper domain size was fabricated by modulating crystallization kinetics via combining the solution state and TA treatment.

The relationship between morphology and device performance

As we mentioned previously, PBDB-T and N2200 crystallized simultaneously when the active layer is processed from solution at ambient temperature (20°C). In addition, the device based on this active layer was labeled Sim-Device. When the active layer was processed from solution with 80°C and then followed by TA treatment at 140°C, N2200 would crystallize at the film-forming process and PBDB-T would crystallize in the following TA process. The device fabricated through the above strategy was labeled Sep-Device. The J-V characteristics under one sun illumination and the photovoltaic parameters of Sim-Device and Sep-Device were summarized in Table 1 and Figure 6A, and the corresponding statistical analysis curves are shown in Figure S5. The Sim-Device exhibits a short-circuit current density (J_{sc}) and open-circuit voltage (V_{oc}) of 10.86 mA cm^{-2} and 0.86 V, respectively, and a fill factor (FF) of 0.65, resulting in a PCE of 6.07%. The Sep-Device gives a similar V_{oc} of 0.84 V but remarkably higher J_{sc} and FF of 13.48 mA cm^{-2} and 0.67, respectively, with an overall efficiency of 7.59%, which is among the highest PCEs reported in the literature for devices based on PBDB-T/N2200 blend. Meanwhile, the photocurrents calculated from the integration of external quantum efficiency (EQE) responses are well matched with the measured J_{sc} within 3% error (Figure 6B). Additionally, the EQE of Sep-Device shows significant improvements throughout the whole spectral range, indicating the efficient exciton dissociation and charge transport.

The plot of effective voltage (V_{eff}) vs photogenerated current density (J_{ph}) shows the efficiency of exciton dissociation ($P_{diss} = J_{ph}/J_{sat}$) (Figure 6C), where J_{sat} is the saturation photocurrent density at high voltage (V_{eff} = 5 V) (Yang et al., 2021). After calculating, the values of P_{diss} for the Sim-Device and Sep-Device were 88 and 95% under short-circuit condition, respectively. The increased P_{diss} should be mainly attributed to the reduced domain size. As we mentioned previously, when PBDB-T and N2200 crystallized at different stages, the domain size decreased from 16.9 nm to 10.8 nm (Figures 3 and 5), which resulted in more excitons diffusing to the interface of D/A and generating more free carriers.

Moreover, the increased device performance can be partly explained by the charge carrier dynamics. The probability of bimolecular recombination was measured by the light–intensity dependencies as well (Figure 6D). The correlation between J_{sc} and light intensity follows the equation $J_{sc} \propto P^{\alpha}$, in which p is the light intensity and α is the exponential factor (Liang et al., 2021). These data are plotted on a log-log scale, and the values of α were calculated as 0.953 and 0.981 for Sim-Device and Sep-Device, respectively. The result suggests Sep-Device could suppress bimolecular recombination, which is in good agreement with the higher FF. The suppressed bimolecular recombination must originate from the improved carrier transport behavior. The charge-carrier mobility was measured using SCLC method (Figure S6) and the obtained data were summarized in Table 1. For a Sim-Device, the values of μ_h and μ_e are 2.64×10^{-4} cm^2 V^{-1} s^{-1} and 7.12×10^{-5} cm^2 V^{-1} s^{-1}, respectively. However, for Sep-Device, the carrier mobility increased (μ_h = 4.53×10^{-3} cm^2 V^{-1} s^{-1} and μ_e = 2.34×10^{-4} cm^2 V^{-1} s^{-1}), which may ascribe to the formation of impeccable interpenetrating network. Furthermore, the μ_h/μ_e ratio of Sep-Device is lower than the one of Sim-Device, which means a more balanced charge transport in Sep-Device (Liu et al., 2018; Liang et al., 2018). Consequently, the increased charge carrier mobility and optimized balanced charge transport in Sep-Device ensured the
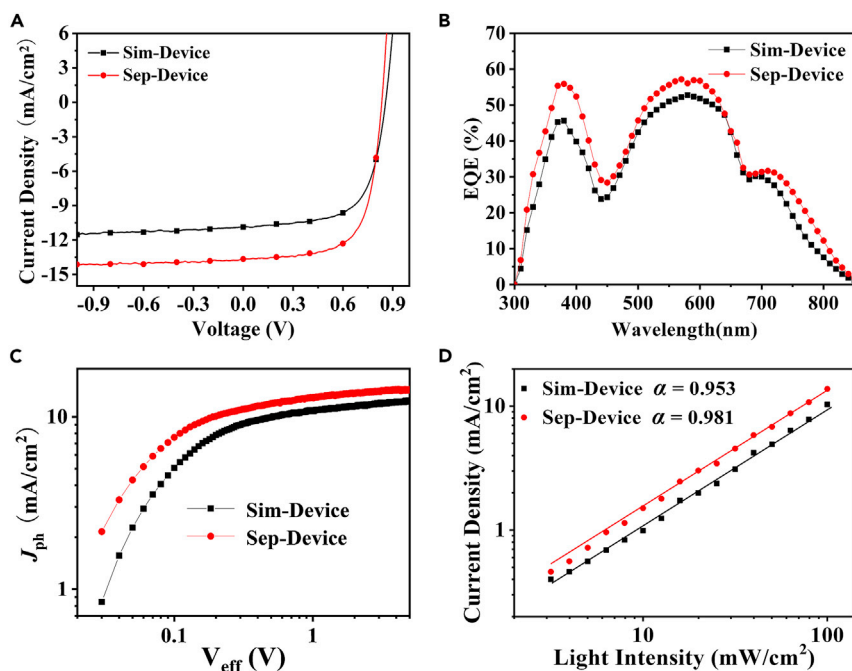
Figure 6. Photovoltaic properties of devices
(A) J-V curves.
(B) EQE curves.
(C and D) J_{ph} vs V_{eff} and J_{sc} on light intensity of Sim-Device and Sep-Device.

efficient charge transport and collection, thus leading to an improved FF and boosting the device performance. The balanced charge transport in Sep-Device may result from the impeccable interpenetrating network with high crystallinity as shown in AFM images.

Conclusions

In summary, a strategy that donor and acceptor crystallize at different stages was proposed. Firstly, the solution temperature was finely adjusted according to the theory of Flory, which promotes only N2200 to form the pre-aggregations in PBDB-T/N2200 solution. Because of the "memory effect" of solution, the pre-aggregations would act as nucleus and promote N2200 to form crystalline framework during film-forming process, while PBDB-T existed mainly in amorphous state and filled the gaps of the framework of N2200. Then, TA treatment with well-designed temperature was employed, which induced PBDB-T to crystallize under the confinement of N2200 crystalline network without enlarging domain size. This strategy could reduce the driving force of phase separation without the expense of crystallinity, thus leading to a highly crystalline phase separation structure with small domain size. Employing this strategy, the domain size of PBDB-T/N2200 blend decreased from the initial 16.9 nm–10.8 nm through combining the regulation of the solution state and TA treatment, which boosted the PCE from 6.07% to 7.59%. Moreover, the relationship between solution state and domain size of film in crystalline-crystalline blend system was established: if both donor and acceptor aggregate in solution, it tends to form a large phase separation. If neither donor nor acceptor form pre-aggregation in solution, a small domain size can be obtained. If only one component is aggregated in solution, it tends to form a suitable domain size. According to the relationships, a possible phase diagram was also depicted, which may be a guide to directly control the domain size of all-PSCs through solution state.

Limitations of the study

There are many kinetics and thermodynamics methods to efficiently adjust the domain size in all-PSCs. These methods can be explored to further improve the device performance.

STAR★METHODS

Detailed methods are provided in the online version of this paper and include the following:

SUPPLEMENTAL INFORMATION

Supplemental information can be found online at https://doi.org/10.1016/j.isci.2022.104090.

AUTHOR CONTRIBUTIONS

W.H., Q.J.L., and J.G.L. conceived and designed the work. C.P.S. carried out the device fabrication and performed the electrical measurements. Y.K.Y., P.X.W., and K.W. conducted the characterization of morphology. J.G.L. wrote the manuscript. H.D.L and J.G.L. analyzed and interpreted the data. All authors discussed the results and commented on the final manuscript.

DECLARATION OF INTERESTS

The authors declare no competing interests.

REFERENCES

Bi, Z., Naveed, H.B., Mao, Y., Yan, H., and Ma, W. (2018). Importance of nucleation during morphology evolution of the blade-cast PffBT4T-2OD-based organic solar cells. Macromolecules 51, 6682–6691. https://doi.org/10.1021/acs.macromol.8b01156.

Binder, K., and Stauffer, D. (1976). Statistical theory of nucleation, condensation and coagulation. Adv. Phys. 25, 343–396. https://doi.org/10.1080/00018737600101402.

Chou, K.W., Yan, B., Li, R., Li, E.Q., Zhao, K., Anjum, D.H., Alvarez, S., Gassaway, R., Biocca, A., Thoroddsen, S.T., et al. (2013). Solar cells: spin-cast bulk heterojunction solar cells: a dynamical investigation. Adv. Mater. 25, 1805. https://doi.org/10.1002/adma.201370082.

Chen, H., Zhang, R., Chen, X., Zeng, G., Kobera, L., Abbrent, S., Zhang, B., Chen, W., Xu, G., Oh, J., et al. (2021). A guest-assisted molecular-organization approach for >17% efficiency organic solar cells using environmentally friendly solvents. Nat. Energy 6, 1045–1053. https://doi.org/10.1038/s41560-021-00923-5.

Eastham, N.D., Dudnik, A.S., Aldrich, T.J., Manley, E.F., Fauvell, T.J., Hartnett, P.E., Wasielewski, M.R., Chen, L.X., Melkonyan, F.S., Facchetti, A., et al. (2017). Small molecule acceptor and polymer donor crystallinity and aggregation effects on microstructure templating: understanding photovoltaic response in fullerene-free solar cells. Chem. Mater. 29, 4432–4444. https://doi.org/10.1021/acs.chemmater.7b00964.

Fan, Q., Fu, H., Wu, Q., Wu, Z., Lin, F., Zhu, Z., Min, J., Woo, H.Y., and Jen, A.K.Y. (2021). Multi-selenophene-containing narrow bandgap polymer acceptors for all-polymer solar cells with over 15 % efficiency and high reproducibility. Angew. Chem. Int. Ed. 60, 15935–15943. https://doi.org/10.1002/anie.202101577.

Fu, J., Chen, S., Yang, K., Jung, S., Lv, J., Lan, L., Chen, H., Hu, D., Yang, Q., Duan, T., et al. (2020). A "σ-hole"-containing volatile solid additive enabling 16.5% efficiency organic solar cells. iScience 23, 100965. https://doi.org/10.1016/j.isci.2020.100965.

Fu, H., Li, Y., Yu, J., Wu, Z., Fan, Q., Lin, F., Woo, H.Y., Gao, F., Zhu, Z., and Jen, A.K.Y. (2021). High efficiency (15.8%) all-polymer solar cells enabled by a regioregular narrow bandgap polymer acceptor. J. Am. Chem. Soc. 143, 2665–2670. https://doi.org/10.1021/jacs.0c12527.

Gu, X., Yan, H., Kurosawa, T., Schroeder, B.C., Gu, K.L., Zhou, Y., To, J.W.F., Oosterhout, S.D., Savikhin, V., Molina-Lopez, F., et al. (2016). Comparison of the morphology development of polymer-fullerene and polymer-polymer solar cells during solution-shearing blade coating. Adv. Energy Mater. 6, 1601225. https://doi.org/10.1002/aenm.201601225.

Kang, H., Uddin, M.A., Lee, C., Kim, K.-H., Nguyen, T.L., Lee, W., Li, Y., Wang, C., Woo, H.Y., and Kim, B.J. (2015). Determining the role of polymer molecular weight for high-performance all-polymer solar cells: its effect on polymer

aggregation and phase separation. J. Am. Chem. Soc. *137*, 2359–2365. https://doi.org/10.1021/ja5123182.

Kurosawa, T., Gu, X., Gu, K.L., Zhou, Y., Yan, H., Wang, C., Wang, G.J.N., Toney, M.F., and Bao, Z. (2018). Understanding the impact of oligomeric polystyrene side chain arrangement on the all-polymer solar cell performance. Adv. Energy Mater. *8*, 1701552. https://doi.org/10.1002/aenm.201701552.

Lee, C., Li, Y., Lee, W., Lee, Y., Choi, J., Kim, T., Wang, C., Gomez, E.D., Woo, H.Y., and Kim, B.J. (2016). Correlation between phase-separated domain sizes of active layer and photovoltaic performances in all-polymer solar cells. Macromolecules *49*, 5051–5058. https://doi.org/10.1021/acs.macromol.6b01069.

Li, Z., Xu, X., Zhang, W., Meng, X., Ma, W., Yartsev, A., Inganäs, O., Andersson, M.R., Janssen, R.A.J., and Wang, E. (2016). High performance all-polymer solar cells by synergistic effects of fine-tuned crystallinity and solvent annealing. J. Am. Chem. Soc. *138*, 10935–10944. https://doi.org/10.1021/jacs.6b04822.

Li, Y., Liu, H., Wu, J., Tang, H., Wang, H., Yang, Q., Fu, Y., and Xie, Z. (2021). Additive and high-temperature processing boost the photovoltaic performance of nonfullerene organic solar cells fabricated with blade coating and nonhalogenated solvents. ACS Appl. Mater. Interfaces *13*, 10239–10248. https://doi.org/10.1021/acsami.0c23035.

Liang, Q., Han, J., Song, C., Wang, Z., Xin, J., Yu, X., Xie, Z., Ma, W., Liu, J., and Han, Y. (2017). Tuning molecule diffusion to control the phase separation of the *p*-DTS(FBTTH2)2/EP-PDI blend system via thermal annealing. J. Mater. Chem. C *5*, 6842–6851. https://doi.org/10.1039/c7tc01763d.

Liang, Q., Han, J., Song, C., Yu, X., Smilgies, D.-M., Zhao, K., Liu, J., and Han, Y. (2018). Reducing the confinement of PBDB-T to ITIC to improve the crystallinity of PBDB-T/ITIC blends. J. Mater. Chem. A *6*, 15610–15620. https://doi.org/10.1039/c8ta05892j.

Liang, Q., Jiao, X., Yan, Y., Xie, Z., Lu, G., Liu, J., and Han, Y. (2019). Separating crystallization process of P3HT and O-IDTBR to construct highly crystalline interpenetrating network with optimized vertical phase separation. Adv. Funct. Mater. *29*, 1807591. https://doi.org/10.1002/adfm.201807591.

Liang, Q., Hu, Z., Yao, J., Wu, Z., Ding, Z., Zhao, K., Jiao, X., Liu, J., and Huang, W. (2021). Blending donors with different molecular weights: an efficient strategy to resolve the conflict between coherence length and intermixed phase in polymer/nonfullerene solar cells. Small *17*, 2103804. https://doi.org/10.1002/smll.202103804.

Liu, J., Gao, X., Sun, Y., and Han, Y. (2013). A quasi-ordered bulk heterojunction of P3HT/PCBM solar cells fabricated by zone-casting. Sol. Energy Mater. Sol. Cells *117*, 421–428. https://doi.org/10.1016/j.solmat.2013.06.031.

Liu, Y., Zhao, J., Li, Z., Mu, C., Ma, W., Hu, H., Jiang, K., Lin, H., Ade, H., and Yan, H. (2014). Aggregation and morphology control enables multiple cases of high-efficiency polymer solar cells. Nat. Commun. *5*, 5293. https://doi.org/10.1038/ncomms6293.

Liu, J., Tang, B., Liang, Q., Han, Y., Xie, Z., and Liu, J. (2017). Dual Förster resonance energy transfer and morphology control to boost the power conversion efficiency of all-polymer OPVs. RSC Adv. *7*, 13289–13298. https://doi.org/10.1039/c7ra00244k.

Liu, J., Han, J., Liang, Q., Xin, J., Tang, Y., Ma, W., Yu, X., and Han, Y. (2018). Balancing crystal size in small-molecule nonfullerene solar cells through fine-tuning the film-forming kinetics to fabricate interpenetrating network. ACS Omega *3*, 7603–7612. https://doi.org/10.1021/acsomega.8b01162.

Liu, B., Wang, J., Sun, H., Wu, Z., Yao, C., Liao, Q., Wei, Z., Yang, W., Zhang, X., Meng, H., et al. (2020a). A terpolymer acceptor enabling all-polymer solar cells with a broad donor:acceptor composition tolerance and enhanced stability. Sol. RRL *4*, 2000436. https://doi.org/10.1002/solr.202000436.

Liu, J., Zeng, S., Zhang, Z., Peng, J., and Liang, Q. (2020b). Optimizing the phase-separated domain size of the active layer via sequential crystallization in all-polymer solar cells. J. Phys. Chem. Lett. *11*, 2314–2321. https://doi.org/10.1021/acs.jpclett.0c00249.

Lombeck, F., Sepe, A., Thomann, R., Friend, R.H., and Sommer, M. (2016). Compatibilization of all-conjugated polymer blends for organic photovoltaics. ACS Nano *10*, 8087–8096. https://doi.org/10.1021/acsnano.6b04244.

Luo, Z., Liu, T., Ma, R., Xiao, Y., Zhan, L., Zhang, G., Sun, H., Ni, F., Chai, G., Wang, J., et al. (2020). Precisely controlling the position of bromine on the end group enables well-regular polymer acceptors for all-polymer solar cells with efficiencies over 15%. Adv. Mater. *32*, 2005942. https://doi.org/10.1002/adma.202005942.

Ma, W., Yang, G., Jiang, K., Carpenter, J.H., Wu, Y., Meng, X., McAfee, T., Zhao, J., Zhu, C., Wang, C., et al. (2015). Organic solar cells: influence of processing parameters and molecular weight on the morphology and properties of high-performance PffBT4T-2OD:PC71BM organic solar cells. Adv. Energy Mater. *5*, 1501400. https://doi.org/10.1002/aenm.201570126.

Ma, R., Yu, J., Liu, T., Zhang, G., Xiao, Y., Luo, Z., Chai, G., Chen, Y., Fan, Q., Su, W., et al. (2021). All-polymer solar cells with over 16% efficiency and enhanced stability enabled by compatible solvent and polymer additives. Aggregate, e58. https://doi.org/10.1002/agt2.58.

Machui, F., and Brabec, C.J. (2013). Solubility, Miscibility, and the Impact on Solid-State Morphology (Wiley-VCH).

Mori, H., Takahashi, R., Hyodo, K., Nishinaga, S., Sawanaka, Y., and Nishihara, Y. (2018). Phenanthrodithiophene (PDT)–difluorobenzothiadiazole (DFBT) copolymers: effect on molecular orientation and solar cell performance of alkyl substitution onto a PDT core. Macromolecules *51*, 1357–1369. https://doi.org/10.1021/acs.macromol.7b02734.

Muthukumar, M. (2004). Nucleation in polymer crystallization. Adv. Chem. Phys. *128*, 1–63. https://doi.org/10.1002/0471484237.ch1.

Neupane, U., Bahrami, B., Biesecker, M., Baroughi, M.F., and Qiao, Q. (2017). Kinetic Monte Carlo modeling on organic solar cells: domain size, donor-acceptor ratio and thickness. Nano Energy *35*, 128–137. https://doi.org/10.1016/j.nanoen.2017.03.041.

Qian, D., Ye, L., Zhang, M., Liang, Y., Li, L., Huang, Y., Guo, X., Zhang, S., Tan, Z.A., and Hou, J. (2012). Design, application, and morphology study of a new photovoltaic polymer with strong aggregation in solution state. Macromolecules *45*, 9611–9617. https://doi.org/10.1021/ma301900h.

Reichenberger, M., Kroh, D., Matrone, G.M.M., Schötz, K., Pröller, S., Filonik, O., Thordardottir, M.E., Herzig, E.M., Bässler, H., Stingelin, N., and Köhler, A. (2018). Controlling aggregate formation in conjugated polymers by spin-coating below the critical temperature of the disorder–order transition. J. Polym. Sci. B Polym. Phys. *56*, 532–542. https://doi.org/10.1002/polb.24562.

Reiter, G. (2014). Some unique features of polymer crystallisation. Chem. Soc. Rev. *43*, 2055–2065. https://doi.org/10.1039/c3cs60306g.

Sen, K.S., Duarte Campos, D.F., Köpf, M., Blaeser, A., and Fischer, H. (2018). The effect of addition of calcium phosphate particles to hydrogel-based composite materials on stiffness and differentiation of mesenchymal stromal cells toward osteogenesis. Adv. Healthc. Mater. *7*, 1800343. https://doi.org/10.1002/adhm.201800343.

Song, C., Qu, Y., Liu, J., and Han, Y. (2018). Phase-separated mechanism and morphological control of all-polymer solar cells. Acta Polym. Sin. *2*, 145–163. https://doi.org/10.11777/j.issn1000-3304.2018.17236.

Song, W., Peng, R., Huang, L., Liu, C., Fanady, B., Lei, T., Hong, L., Ge, J., Facchetti, A., and Ge, Z. (2020). Over 14% efficiency folding-flexible ITO-free organic solar cells enabled by eco-friendly acid-processed electrodes. iScience *23*, 100981. https://doi.org/10.1016/j.isci.2020.100981.

Spano, F.C. (2010). The spectral signatures of frenkel polarons in H- and J-aggregates. Acc. Chem. Res. *43*, 429–439. https://doi.org/10.1021/ar900233v.

Spano, F.C., and Yamagata, H. (2011). Vibronic coupling in J-aggregates and beyond: a direct means of determining the exciton coherence length from the photoluminescence spectrum. J. Phys. Chem. B *115*, 5133–5143. https://doi.org/10.1021/jp104752k.

Steyrleuthner, R., Schubert, M., Howard, I., Klaumünzer, B., Schilling, K., Chen, Z., Saalfrank, P., Laquai, F., Facchetti, A., and Neher, D. (2012). Aggregation in a high-mobility n-type low-bandgap copolymer with implications on semicrystalline morphology. J. Am. Chem. Soc. *134*, 18303–18317. https://doi.org/10.1021/ja306844f.

Sun, R., Wang, W., Yu, H., Chen, Z., Xia, X., Shen, H., Guo, J., Shi, M., Zheng, Y., Wu, Y., et al. (2021). Achieving over 17% efficiency of ternary all-polymer solar cells with two well-compatible polymer acceptors. Joule *5*, 1548–1565. https://doi.org/10.1016/j.joule.2021.04.007.

Veenstra, S.C., Loos, J., and Kroon, J.M. (2007). Nanoscale structure of solar cells based on pure conjugated polymer blends. Prog. Photovolt. 15, 727–740. https://doi.org/10.1002/pip.796.

Wang, N., Long, X., Ding, Z., Feng, J., Lin, B., Ma, W., Dou, C., Liu, J., and Wang, L. (2019). Improving active layer morphology of all-polymer solar cells by dissolving the two polymers individually. Macromolecules 52, 2402–2410. https://doi.org/10.1021/acs.macromol.9b00057.

Wang, N., Yu, Y., Zhao, R., Ding, Z., Liu, J., and Wang, L. (2020). Improving active layer morphology of all-polymer solar cells by solution temperature. Macromolecules 53, 3325–3331. https://doi.org/10.1021/acs.macromol.0c00633.

Xu, Y., Yuan, J., Zhou, S., Seifrid, M., Ying, L., Li, B., Huang, F., Bazan, G.C., and Ma, W. (2019). Ambient processable and stable all-polymer organic solar cells. Adv. Funct. Mater. 29, 1806747. https://doi.org/10.1002/adfm.201806747.

Yang, C., Yu, R., Liu, C., Li, H., Zhang, S., and Hou, J. (2021). Achieving over 10 % efficiency in poly(3-hexylthiophene)-based organic solar cells via solid additives. ChemSusChem 14, 3607–3613. https://doi.org/10.1002/cssc.202100627.

Ye, L., Zhao, W., Li, S., Mukherjee, S., Carpenter, J.H., Awartani, O., Jiao, X., Hou, J., and Ade, H. (2017). High-efficiency nonfullerene organic solar cells: critical factors that affect complex multi-length scale morphology and device performance. Adv. Energy Mater. 7, 1602000. https://doi.org/10.1002/aenm.201602000.

Ye, L., Li, S., Liu, X., Zhang, S., Ghasemi, M., Xiong, Y., Hou, J., and Ade, H. (2019a). Quenching to the percolation threshold in organic solar cells. Joule 3, 443–458. https://doi.org/10.1016/j.joule.2018.11.006.

Ye, L., Xiong, Y., Chen, Z., Zhang, Q., Fei, Z., Henry, R., Heeney, M., O'Connor, B.T., You, W., and Ade, H. (2019b). Sequential deposition of organic films with eco-compatible solvents improves performance and enables over 12%-efficiency nonfullerene solar cells. Adv. Mater. 31, 1808153. https://doi.org/10.1002/adma.201808153.

Zhang, Z.-G., and Li, Y. (2021). Polymerized small-molecule acceptors for high-performance all-polymer solar cells. Angew. Chem. Int. Ed. 60, 4422–4433. https://doi.org/10.1002/anie.202009666.

Zhang, R., Yang, H., Zhou, K., Zhang, J., Yu, X., Liu, J., and Han, Y. (2016). Molecular orientation and phase separation by controlling chain segment and molecule movement in P3HT/N2200 blends. Macromolecules 49, 6987–6996. https://doi.org/10.1021/acs.macromol.6b01526.

Zhang, J., Xie, S., Lu, Z., Wu, Y., Xiao, H., Zhang, X., Li, G., Li, C., Chen, X., Ma, W., and Bo, Z. (2018). Influence of substrate temperature on the film morphology and photovoltaic performance of non-fullerene organic solar cells. Sol. Energy Mater. Sol. Cells 174, 1–6. https://doi.org/10.1016/j.solmat.2017.07.012.

Zhang, Q., Yuan, X., Feng, Y., Larson, B.W., Su, G.M., Maung Maung, Y., Rujisamphan, N., Li, Y., Yuan, J., and Ma, W. (2020). Understanding the interplay of transport-morphology-performance in PBDB-T-based polymer solar cells. Sol. RRL 4, 1900524. https://doi.org/10.1002/solr.201900524.

Zhang, Y., Wang, N., Wang, Y., Zhang, J., Liu, J., and Wang, L. (2021a). All-polymer indoor photovoltaic modules. iScience 24, 103104. https://doi.org/10.1016/j.isci.2021.103104.

Zhang, L., Jia, T., Pan, L., Wu, B., Wang, Z., Gao, K., Liu, F., Duan, C., Huang, F., and Cao, Y. (2021b). 15.4% efficiency all-polymer solar cells. Sci. China Chem. 64, 408–412. https://doi.org/10.1007/s11426-020-9935-2.

Zhang, Z.-G., Bai, Y., and Li, Y. (2021c). Benzotriazole based 2D-conjugated polymer donors for high performance polymer solar cells. Chin. J. Polym. Sci. 39, 1–13. https://doi.org/10.1007/s10118-020-2496-5.

Zhang, J., Jia, T., Tan, C.-H., Zhang, K., Ren, M., Dong, S., Xu, Q., Huang, F., and Cao, Y. (2021d). Nonhalogenated-solvent-processed high-performance all-polymer solar cell with efficiency over 14%. Sol. RRL 5, 2100076. https://doi.org/10.1002/solr.202100076.

Zhao, H., Naveed, H.B., Lin, B., Zhou, X., Yuan, J., Zhou, K., Wu, H., Guo, R., Scheel, M.A., Chumakov, A., et al. (2020). Hot hydrocarbon-solvent slot-die coating enables high-efficiency organic solar cells with temperature-dependent aggregation behavior. Adv. Mater. 32, e2002302. https://doi.org/10.1002/adma.202002302.

Zhou, K., Xian, K., and Ye, L. (2022). Morphology control in high-efficiency all-polymer solar cells. InfoMat. https://doi.org/10.1002/inf2.12270.

Zhu, Y., Gadisa, A., Peng, Z., Ghasemi, M., Ye, L., Xu, Z., Zhao, S., and Ade, H. (2019). Rational strategy to stabilize an unstable high-efficiency binary nonfullerene organic solar cells with a third component. Adv. Energy Mater. 9, 1900376. https://doi.org/10.1002/aenm.201900376.

STAR★METHODS

KEY RESOURCES TABLE

REAGENT or RESOURCE	SOURCE	IDENTIFIER
Chemicals, peptides, and recombinant proteins		
PBDB-T	Solarmer Materials Inc	ZJ401A
N2200	Polyera Corporation	YY15046CH
PEDOT:PSS	H. C. Starck Inc	Clevios VP Al 4083
Chlorobenzene, AR	Sigma-Aldrich	284,513
Critical commercial assays		
Spectrometers	AvaLight-Hal	Ava-3648
Atomic Force Microscope	Seiko Instruments Inc	SPI3800N
Grazing Incidence Small Angle X-ray Scattering (GISAXS)	Shanghai Synchrotron Facility (SSRF)	Beamline 14B
Grazing Incidence X-ray Diffraction (GIXD)	Bruker Corporation	D8 Discover Reflector
Other		
General Purpose Digital Source Meter	Keithley	2400
Solar Cell Spectral Response Measurement System	Enlitech Co., Ltd	QE-R 3011
Solar Simulator	SAN-EI Electric Co., Ltd	XES-40S2-CE

RESOURCE AVAILABILITY

Lead contact

Further information and requests for resources and reagents should be directed to and will be fulfilled by the lead contact, Qiuju Liang (qiujuliang@nwpu.edu.cn).

Materials availability

This study did not generate new unique reagents.

Data and code availability

This paper did not generate and does not report original code. The Critical assays and chemicals used in this study are described in the method details and key resources table. All data reported in this paper will be shared by the lead contact upon request. Any additional information required to reanalyze the data reported in this work paper is available from the lead contact upon the reasonable request.

METHOD DETAILS

Materials

PBDB-T (M_n = 72 kDa, PDI = 2.3) were purchased from Solarmer Materials Inc and N2200 (M_n = 38, PDI = 2.2) were purchased from Polyera Corporation. Anhydrous solvent chlorobenzene (CB) was purchased from Sigma-Aldrich. All chemicals were used as received.

Device fabrication

Organic solar cells were fabricated in the configuration of indium tin oxide on indium tin oxide (ITO)/ZnO/PBDB-T:N2200/MoO$_3$/Al. The cleaned ITO glass substrates were treated with UV-ozone for 25 min. Subsequently, ZnO layer was spin-coated on the top of the ITO glass and dried at 200°C for 60 min. The PBDB-T:N2200 solution with a total concentration of 16 mg mL^{-1} was spin-cast on top of the ZnO layer to produce active layer with thickness of 110 nm. The thickness of active layers was adjusted through regulating the rate of spin-coating. Finally, a bilayer structure of MoO$_3$ (10 nm)/Al (100 nm) was deposited on top of the active layer by thermal evaporation in a vacuum of 2 × 10^{-4} Pa. Four solar cells, each with an active area of 7.2 mm^2, were fabricated per ITO glass substrate.

Characterization

The absorption of the sample was recorded by UV-vis absorption spectroscopy (AvaLight-Hal) with halogen lamp source. The morphology of PBDB-T/N2200 film was characterized by using atomic force microscopy (AFM). AFM was utilized to study the surface topography of the films. Images were obtained by using a SPI3800N AFM (Seiko Instruments Inc., Japan) with a Si tip with a spring constant of 3 N/m. The phase separation of blended films was characterized by the grazing incidence small angle X-ray scattering (GISAXS) (Shanghai Synchrotron Facility (SSRF) beamline 14B using Huber diffractometer and a scintillation counter). The films were first aligned and then their GISAXS were measured in out-of-plane direction with incident angle of 0.18. The scan range was from 0.18 to 0.48 in 0.018 step. To eliminate the influence of X-ray wavelength and reflection, the data were plotted with $q \sim Iq^2$. The thin film crystallinity was investigated by Out-of-plane grazing incidence X-ray diffraction (GIXD). GIXD data were obtained on a Bruker D8 Discover Reflector (Cu Kα, λ = 1.54 Å) under 40 kV and 40 mA tube current. The scanning speed is 5 s per step with 0.05° step size (2θ). The measurements were obtained in a scanning interval of 2θ between 2 and 30°. Current density-voltage (J-V) characteristics of the PV cells were measured using a computer controlled Keithley 236 source meter under AM1.5G illumination from a calibrated solar simulator with irradiation intensity of 100 mW/cm^2. The external quantum efficiency (EQE) of the PV cells was measured with a lock-in amplifier at a chopping frequency of 280 Hz during illumination with the monochromatic light from a xenon lamp. The charge-carrier mobility was characterized by using the space-charge-limited current (SCLC) method. The hole-only and electron-only device structures are ITO/PEDOT:PSS/active layer/MoO$_3$/Al and ZnO/active layer/PFNBr/Al, respectively.

QUANTIFICATION AND STATISTICAL ANALYSIS

To compare the device performance changes, the photovoltaic parameters reported in this work are the average values of 16 devices under the same conditions.